

This is a repository copy of *Morphology formation in binary mixtures upon gradual destabilisation*.

White Rose Research Online URL for this paper:

<https://eprints.whiterose.ac.uk/154074/>

Version: Accepted Version

Article:

Schaefer, Charley, Paquay, Stefan and McLeish, Tom C.B. orcid.org/0000-0002-2025-0299 (2019) Morphology formation in binary mixtures upon gradual destabilisation. *Soft Matter*. pp. 8450-8458. ISSN 1744-683X

<https://doi.org/10.1039/c9sm01344j>

Reuse

Items deposited in White Rose Research Online are protected by copyright, with all rights reserved unless indicated otherwise. They may be downloaded and/or printed for private study, or other acts as permitted by national copyright laws. The publisher or other rights holders may allow further reproduction and re-use of the full text version. This is indicated by the licence information on the White Rose Research Online record for the item.

Takedown

If you consider content in White Rose Research Online to be in breach of UK law, please notify us by emailing eprints@whiterose.ac.uk including the URL of the record and the reason for the withdrawal request.

Cite this: DOI: 10.1039/xxxxxxxxxx

Morphology Formation in Binary Mixtures upon Gradual Destabilisation

 Charley Schaefer^{*,a}, Stefan Paquay^b, and Tom C. B. McLeish^a

Received Date

Accepted Date

DOI: 10.1039/xxxxxxxxxx

www.rsc.org/journalname

Spontaneous liquid-liquid phase separation is commonly understood in terms of phenomenological mean-field theories. These theories correctly predict the structural features of the fluid at sufficiently long time scales and wavelengths. However, these conditions are not met in various examples in biology and materials science where the mixture is slowly destabilised, and phase separation takes place close to the critical point. We propose a mechanism of pretransitional structuring taking place prior to reaching the miscibility gap, and use this to predict the characteristic length scale of the emerging phase-separated morphology. This mechanism quantitatively agrees with previously published experiments, as well as with our kinetic Monte Carlo and molecular dynamics simulations of a binary surface fluid. We discuss how the predictions of this theory vary for simple fluids, systems with non-conserved order parameters (e.g., liquid crystals and reactive mixtures), and systems with phase-separating active particles.

1 Introduction

In recent years, ‘liquid-liquid phase condensation’ (LLPS) has received a lot of attention due to its relevance to various biological processes¹. LLPS appears to have features that have previously been observed in various examples in soft matter, such as systems with a ‘non-conserved order parameter’, such as mixtures with chemical reactions or with liquid-crystalline domains^{2–4}, ‘active systems’ with microswimmers⁵, and systems with a ‘conserved order parameter’ like water-and-oil mixtures^{6–8}. In these types of systems, the origin of phase separation can be phenomenologically understood in terms of a thermodynamic free energy, and the arrested growth of droplets can be understood in terms of viscoelasticity⁹, hydrodynamics^{10,11}, chemical reactions^{10–13}, turbulent flow¹⁴, the presence of a surfactant¹⁵, or active particles⁵. However, these mean-field models break down under conditions of marginal stability (i.e., near the critical point), which is speculated to occur in biology¹⁶, but is also encountered in materials science. Indeed, under conditions of a gradual temperature or a concentration quench of a simple binary mixture^{17–26} it was experimentally⁶ and theoretically^{18,23} shown that mean-field theory fails to predict how the emerging morphology depends on the quench rate. Here, we rationalise this in terms of universal scaling theory²⁷, of which the predictions are not limited to the simple binary mixture considered in the present work, but can also be applied to non-conserved and active systems.

Before presenting this argument, we first emphasize that mean-field theory is valid in case that a mixture is sufficiently unstable. Indeed, according to mean-field theory, a demixed structure spontaneously emerges if the mixture is deeply quenched within the spinodal region of the phase diagram. Under this condition, there is no activation barrier and heterogeneities are amplified as time proceeds. The fastest growing wavelength is sufficiently short for fast diffusion and sufficiently large to overcome surface tension.

However, if the mixture is slowly and steadily quenched from initially stable conditions into the miscibility gap of the phase diagram, conditions of marginal stability are crossed. If we ignore the breakdown of mean-field theory (or merely correct for thermal fluctuations according to the fluctuation-dissipation theorem^{22,28–31}) and follow its predictions, we expect that the emerging length scale is infinite at the spinodal, and decreases with the square root of time as the miscibility gap is entered. At the point in time where the largest amplitude grows faster than the quench rate, rapid phase separation takes place. The mean-field prediction is that the emerging length scale decreases with the one-sixth power of the quench rate^{17,19,21,22,24}.

Recently, kinetic Monte Carlo (kMC) simulations of a 2D lattice fluid seemed to indicate that liquid-liquid demixing upon a gradual concentration quench leads to a one-fourth power, rather than one sixth²³. This power-law exponent was interpreted to be originated by the diffusion of material towards nuclei: Phase separation takes place at the point in time where diffusion becomes faster than the rate at which the mean-free path becomes shorter, due to an increasing concentration. While this argument compares the time scale of diffusion-limited nucleation to the quench

* E-mail: charley.schaefer@york.ac.uk

^a Department of Physics, University of York, Heslington, York, YO10 5DD, UK.

^b Martin Fisher School of Physics, Brandeis University, Waltham, MA, USA

rate²³, the power one fourth may also be obtained by comparing the time scale of reaction-limited nucleation to the quench rate³². In that case, the size of the clusters is not coupled to the mean-free path, but to the stability of spherical critical nuclei as described by classical nucleation theory³³. Although both theories seem to agree with the observations, the diffusion-limited nucleation argument seems to be specific to the case studied²³, and a simple classical nucleation theory is inaccurate near the critical point³⁴.

In the present work, we argue that the length scale of a mixture that is slowly destabilised is not determined after the miscibility gap is entered, but actually prior to that, namely by universal critical dynamics²⁷. We propose a mechanism where at early times the correlation length is given by the distance from the critical point, while upon reaching the critical point the correlation length increases with the dynamic critical time exponent z ^{27,35,36}. For slow quenches, the emerging length scale is dictated by the early pretransitional structuring, while for fast quenches the late-stage structuring becomes more important. We will show agreement of the predictions in the slow-quench limit with previously published experiments⁶, and will give support for the fast-quench limit using kinetic Monte Carlo (kMC) and molecular dynamics (MD) simulations of a gradually destabilised binary mixture.

In the following, we present the theory of demixing from the phenomenological (mean-field) point of view, our proposed mechanism beyond the mean-field approximation, and then present the two simulation methods that we will employ. Subsequently, we present our simulation results and briefly discuss the implications of our findings to a broader range of applications.

2 Theory

2.1 Mesoscopic mean-field modelling

The phase separation of a homogeneous mixture with a single phase into a heterogeneous mixture with coexisting phases is thermodynamically understood by a favourable change in free energy. Phenomenologically, an order parameter $-1 \leq \psi \leq 1$ can be assigned to the system (which could be related to the local concentration, magnetisation, orientation vector, etc.), and a dimensionless Landau free-energy density may be assumed*

$$f(\psi) = -\frac{1}{2}a\psi^2 + \frac{1}{4}b\psi^4. \quad (1)$$

Indeed, coexisting phases with $\psi = \pm\sqrt{b/a}$ have a combined free energy $[f(+\sqrt{b/a}) + f(-\sqrt{b/a})]/2$ smaller than that of the homogeneous mixture $f(\psi = 0)$. Here, $a > 0$ and $b > 0$ are phenomenological parameters, to which a physical meaning can be attributed by choosing an appropriate mean-field theory.

While phase separation is driven by the local free energy, it is counteracted by a free-energy penalty for the formation of spatial inhomogeneities of the order parameter (i.e., surface tension). For sufficiently weak spatial gradients, this can be captured using a Van der Waals-type non-local free energy $\kappa/2|\nabla\psi(\mathbf{r})|^2$. Inte-

gration over the system volume gives the Ginzburg-Landau free-energy functional

$$\mathcal{F} = \int d\mathbf{r} \left(f(\psi) + \frac{1}{2}\kappa|\nabla\psi|^2 \right), \quad (2)$$

with \mathbf{r} the dimensionless spatial coordinate, κ a constant often denoted as the ‘square-gradient coefficient’, ‘gradient stiffness’ or ‘elastic constant’. Mass transport is driven by spatial gradients in the chemical potential as $\mathbf{j} = -M\nabla\mu$ ³⁷, where the chemical potential, $\mu \equiv \delta\mathcal{F}/\delta\psi$, is a functional derivative obtained from the Euler-Lagrange equation $\mu = \partial f/\partial\psi - \kappa\nabla \cdot \partial|\nabla\psi|^2/\partial(\nabla\psi) = \partial f/\partial\psi - \kappa\nabla^2\psi$. Further, M is the mobility, and is related to the cooperative diffusion coefficient as $D = M\partial\mu/\partial\psi$.

Taken into account that the order parameter is locally conserved[†], its time evolution is described by $\partial\psi/\partial t = -\nabla \cdot \mathbf{j}$. By also adding a source term, α , to describe e.g. a concentration quench^{21,22}, and a stochastic term, ξ , that represents thermal fluctuations that obey the fluctuation-dissipation theorem, i.e., $\langle \xi(\mathbf{r}, t) \rangle = 0$ and $\langle \xi(\mathbf{r}, t) \xi(\mathbf{r}', t') \rangle = -2\nabla \cdot M\nabla\delta(\mathbf{r} - \mathbf{r}')\delta(t - t')$ ^{28,29}, we finally have the modified Cahn-Hilliard-Cook (CHC) equation^{27-29,37,38}

$$\frac{\partial\psi}{\partial t} = \nabla \cdot \left(M\nabla \left[f_\psi - \kappa\nabla^2\psi \right] \right) + \xi + \alpha. \quad (3)$$

In order to describe the time evolution of an emerging structure following a gradual quench into the miscibility gap of the phase diagram, we consider a system at time $t = 0$ at the spinodal branch, that is, $\partial^2 f/\partial\psi^2 = 0$. At this stage, the spatial variations of the order parameter are presumably small, i.e., $\psi = \psi^0 + \delta\psi$ with $|\delta\psi| \ll 1$. Hence, we may write $\nabla f_\psi(t) \approx f_{\psi\psi}^0 \nabla\delta\psi(t)$. Assuming a uniform (or absent) source term, Fourier transformation of the CHC equation gives

$$\frac{\partial\hat{\delta\psi}}{\partial t}(q, t) = -q^2 M \left(f_{\psi\psi}(t) + \kappa q^2 \right) \hat{\delta\psi}(q, t) + \hat{\xi}(q, t). \quad (4)$$

For early times after the spinodal is crossed the second order derivative of the free energy is $f_{\psi\psi}(t) \approx -\Gamma t$, with

$$\Gamma \equiv \left. \frac{\partial f_{\psi\psi}}{\partial t} \right|_{t=t_{\text{spinodal}}} \quad (5)$$

the quench rate, i.e., the rate by which the mixture is thermodynamically destabilised. At the spinodal, the dominant structural wavelength is infinite, but decreases as time proceeds and the miscibility gap is entered deeper. This is captured by the wavenumber $q_*(t) \approx \sqrt{(\Gamma/2\kappa)t}$, which reduces the CHC equation to

$$\frac{\partial\hat{\delta\psi}_*}{\partial t/\tau} = \frac{M\Gamma^2}{4\kappa} \tau^3 \left(\frac{t}{\tau} \right)^2 \hat{\delta\psi}_* + \hat{\xi}\tau, \quad (6)$$

with τ the characteristic ‘time lag’ after which the phase-separated structure rapidly emerges ($\ln \delta\psi \propto t^3$). This time scale, and the dominant wavenumber of the emerging structure, depend

* The energies are given in units of thermal energy $k_B T$, with k_B Boltzmann’s constant and T the absolute temperature. The spatial positions/distances are given in units of the smallest length scale in the system, which is in our case the size of a molecule.

† For non-conserved order parameters, such as the orientation vector of liquid crystals (LC), $\nabla \cdot M\nabla$ is replaced by M . In case of LCs, M now represents a rotational rather than a translational mobility.

on the quench rate as¹⁷

$$\tau \propto \Gamma^{-2/3}, \quad q_*(\tau) \propto \Gamma^{1/6}, \quad (7)$$

2.2 Critical fluctuations

The above free-energy functional is accurate if the binary mixture is sufficiently far from the critical point. During a gradual quench, however, phase separation may take place close to the critical point where the correlation length diverges according to critical scaling theory. In a previous combined experimental and theoretical work⁶, it was proposed that after the miscibility gap is entered, the correlation length decreases, and the rate at which this happens sets a time scale where true phase separation sets in. On the other hand, here we propose a mechanism where in the pretransitional regime, i.e., before the miscibility gap is entered, the fluctuations emerge with an increasing length scale. As we will show, in the limit of slow quenches this theory shows excellent quantitative agreement with the experimental findings in Ref.⁶.

In the mechanism that we propose, at the early pretransitional stages before some time t' (which we calculate below), the equilibrium correlation length, ξ_{eq} , remains small and the interdiffusivity D remains finite. Hence, for times $t < t'$ the mixture remains equilibrated and has a dynamic correlation length that is given by

$$\xi = \xi_{\text{eq}} = \xi_{\text{eq}}^0 |\Delta T|^\nu, \quad (8)$$

with ξ_{eq}^0 a constant prefactor, $|\Delta T| \equiv |(T - T_c)/T_c|$ the time-dependent distance from the critical point and ν a critical exponent ($\nu = 1$ in 2D and $\nu \approx 0.63$ in 3D). The distance from the critical point evolves with time, to linear order, as $|\Delta T| = |\Delta T|_0 - \Gamma t$, with $|\Delta T|_0$ the distance at time $t = 0$ and Γ the quench rate.

For late times $t > t'$, but before reaching the critical point at $t'' \equiv |\Delta T|_0/\Gamma$, diffusion becomes too slow to equilibrate the mixture up to the length scale of the equilibrium correlation length. Under this condition, the non-equilibrium correlation length that is present in the system increases via dynamic scaling as^{27,35,36}

$$\xi \propto (t - \tilde{t})^{1/z}, \quad (9)$$

with z again the dynamic scaling exponent and $\tilde{t} < t'$ a time scale that we set such that the derivatives of Eq. (8) and Eq. (9) are continuous at time $t = t'$.

We estimate the crossover time t' and correlation length $\xi(t')$ by equating the two time scales of the problem, namely the time scale needed to relax fluctuations with a wavelength of the order of the equilibrium correlation length, and the time scale by which the correlation length increases. The former is $\tau_D = \xi^2/D$, with the interdiffusivity given by

$$D = D_0 |\Delta T|^{\nu*}, \quad (10)$$

where $\nu* \equiv \nu(1 + z - d)$ and d is the spatial dimensionality. The latter time scale we obtain from the time derivative $(d\xi/dt) \propto \xi_{\text{eq}}^0 |\Delta T|^{-(\nu+1)} \Gamma$ as $\tau_t = \xi_{\text{eq}}^0 / (d\xi/dt)$. By setting $\tau_t = \tau_D$, we find the

distance from the critical point

$$|\Delta T|' \propto \Gamma^{\frac{1}{3\nu+\nu*+1}}, \quad (11)$$

where the crossover takes place, with correlation length

$$\xi(t') \propto \Gamma^{-\frac{\nu}{3\nu+\nu*+1}}, \quad (12)$$

and time scale

$$t' \propto \Gamma^{-(1-\frac{\nu}{3\nu+\nu*+1})}, \quad (13)$$

These scaling relations show that for a slow quench, t'/t'' becomes large and the late-stage structuring in Eq. 9 becomes negligible compared to the late-stage structuring Eq. 8. In this slow-quench limit, we expect Eq. (12) to dominate, giving

$$\xi(t'') \propto \Gamma^{-\frac{\nu}{3\nu+\nu*+1}}. \quad (14)$$

In 3D ($d = 3$, $1/z = 0.326$, and $\nu = 0.63$), this gives $\xi \approx \Gamma^{-0.18}$ and $t' \approx \Gamma^{-0.72}$, which excellently matches with the experimental findings in Ref.⁶. In the fast-quench limit, which will turn out relevant to our simulation results, t'/t'' tends to unity and the late-stage structuring in Eq. 9 will dominate, giving

$$\xi(t'') \propto \Gamma^{-1/z}. \quad (15)$$

We summarise that at time $t = 0$ the correlation length $\xi(t)$ is small, and grows to a finite size $\xi(t'')$ at the time t'' at which the critical point is reached. Upon entering the miscibility gap, a phase-separated structure emerges with a characteristic length scale $R_* \propto \xi(t'')$. At this point in time, the phase diagram is quenched sufficiently far away from the critical point, and further structure development (droplet growth and arrest) is described by mean-field theory / phenomenological modelling. Here, we remark that due to the out-of-equilibrium nature of the continuous quench at any point in time the characteristic length scale remains finite. This implies that if we simulate systems much larger than the final length scale, our simulations do not suffer from any finite-size effects that may be expected from the diverging correlation length at the critical point or the diverging spinodal length scale in mean-field theory.

2.3 Microscopic lattice modelling: kinetic Monte Carlo

The simplest approach is to model a binary A – B mixture on a periodic $N \times N$ square lattice^{12,18,26,39–41}. Each site is either vacant or occupied by A or B. The species have nearest-neighbour interactions ϵ_{AA} , ϵ_{BB} and ϵ_{AB} . Hence, for N_{AA} , N_{BB} and N_{AB} nearest-neighbour pairs, the Hamiltonian is given by

$$\mathcal{H} = \epsilon_{AA} N_{AA} + \epsilon_{AB} N_{AB} + \epsilon_{BB} N_{BB}. \quad (16)$$

At full surface coverage, i.e., for $\theta \equiv (N_A + N_B)/N^2 = 1$, this Hamiltonian can be mapped onto the Ising Hamiltonian. In this case, the components are driven to phase separate if $\epsilon_{AA}/k_B T, \epsilon_{BB}/k_B T > \ln(1 + \sqrt{2})/2 \approx 0.4407^{42}$. For lower concentrations, the critical temperature decreases.

A realistic example for which this lattice model would apply is the adsorption of molecules at the specific lattice sites of a metal surface^{43,44}. In this case, surface diffusion of adsorbants is an activated process where a potential energy barrier has to be overcome. The hop rate then obeys an Arrhenius-type equation

$$W_{\text{hop}} = \nu(T) \exp(-E_{\text{act}}/k_{\text{B}}T), \quad (17)$$

with ν the pre-exponential factor. The temperature dependence of W_{hop} is predominated by the exponential term, and $\nu(T)$ is usually approximated to be isothermal⁴⁴. The activation energy may be approximated by $E_{\text{b}} = E_{\text{b}}^0 + (1/2)\Delta\mathcal{H}$, with E_{b}^0 the activation energy in the limit of low surface coverages and $1/2$ the ‘BEP coefficient’ for simple hopping events⁴³.

We model the response of the lattice fluid to a temperature quench as $T/T_0 = 1 - \Gamma_T t$, with Γ_T a constant cooling rate and T_0 a temperature above the critical temperature. Besides temperature quenches, we also consider isothermal concentration quenches. For that purpose, we initialise the system using an empty surface and let molecular adsorption take place using the rates

$$W_{\theta, \text{A or B}} = \Gamma_{\theta, \text{A or B}}. \quad (18)$$

The resulting macroscopic adsorption rate is given by $d\theta/dt = (1 - \theta)\Gamma_{\theta}$, and the composition of the binary mixture is determined by the ratio between $\Gamma_{\theta, \text{A}}$ and $\Gamma_{\theta, \text{B}}$.

In the present work, we simulate the dynamics using a variable-size-step method kinetic Monte Carlo (kMC) algorithm with a hierarchical selection method.^{44,45} This method is computationally efficient when the number of possible events is limited. For this reason, we use symmetric properties for species A and B: We set the activation barriers equal and set the nearest-neighbour self-interactions to zero $\epsilon_{\text{AA}} = \epsilon_{\text{BB}} = 0$. **The size of the lattice is 512×512 , which is much larger than the out-of-equilibrium correlation length and domain size in our simulations.**

We analyse the results by calculating the order-parameter field $\psi(\mathbf{r}_i)$, with i the lattice coordinate, and where $\psi(i)$ is -1 , 1 or 0 if site i is occupied by A, B, or neither. **We then transform $\psi(\mathbf{r})$ to q space using a 2D Fourier transform, giving $\hat{\psi}(\mathbf{q})$. The characteristic length scale, R_* , manifests itself as a maximum in the cylindrical average, $S(q) = \langle |\hat{\psi}(\mathbf{q})|^2 \rangle$, at $q = q_* = 2\pi/R_*$. As discussed in earlier work^{13,23}, a numerically robust method of determining this value is achieved using the inverse Fourier transform of $S(q)$, yielding the space-correlation function $C(r)$. The minimum of $C(r)$, at $r = R_*$ corresponds to the maximum in $S(q)$. In the remainder, we determine a characteristic length scale R_* from the first minimum in $C(r)$ and probe this measure as a function of time. At the early stages of the quench, R_* gives a measure for the correlation length, and at later stages R_* corresponds to the emerging peak maximum of $S(q)$.**

2.4 Microscopic off-lattice modelling: molecular dynamics

Complementary to the kMC simulations on a lattice, we perform two-dimensional Langevin dynamics simulations of a binary Lennard-Jones liquid with LAMMPS⁴⁶ and its Kokkos package on a single NVidia GTX 1080 Ti. The Lennard-Jones interaction po-

tential between two particles i and j a distance r_{ij} apart is given by

$$U_{\text{AB}}(r_{ij}) = 4\epsilon_{\text{AB}} \left[(\sigma/r_{ij})^{12} - (\sigma/r_{ij})^6 \right] \times u(r_{\text{c,AB}} - r_{ij}),$$

with u a unit step function: $u(x) = 1$ for $x > 0$ and 0 otherwise. In the following, we express distances and energies in the Lennard-Jones units σ and ϵ , respectively, and we express time in terms of the Langevin damping time τ , i.e., the time it takes for the velocity auto-correlation to decay from 1 to $\exp(-1)$. We have set the parameter values to $\epsilon_{\text{AB}} = \epsilon$ independent of the particle types, but $r_{\text{c,11}} = r_{\text{c,22}} = 3\sigma$ while $r_{\text{c,12}} = 2^{1/6}\sigma$. Hence, the interactions between unlike particles is purely repulsive, while the interaction between like particles is attractive. At our reduced Lennard-Jones density of 0.8 particles per σ^2 , this interaction potential drives the phase separation at sufficiently low temperatures.

We numerically solve the dynamics using a temporal step size of 0.005τ , and a planar simulation box with an area A of both $(400\sigma)^2$ and $(800\sigma)^2$ to **confirm the results are not subject to finite-size effects.** get a feel for finite size effects. These simulations involve 128000 particles for $A = (400\sigma)^2$ and 512000 particles for $A = (800\sigma)^2$. As an initial condition, we create a random packing of a single type of particles in the area, and then randomly select half of them and change them to the other type of particles. We run each simulation for five random seeds.

To analyse the results using the same method as for the kMC simulations, we divide the simulation domain into 256×256 (for $A = (400\sigma)^2$) or 512×512 (for $A = (800\sigma)^2$) squares. We count for each of these squares k the number of particles of type A and B, which we denote as $N_{\text{A}}(k)$ and $N_{\text{B}}(k)$. Then, we assign to each square the order parameter $\psi(k) = 1$ if $N_{\text{A}}(k) > N_{\text{B}}(k)$, $\psi(k) = -1$ if $N_{\text{A}}(k) < N_{\text{B}}(k)$, or 0 if $N_{\text{A}}(k) = N_{\text{B}}(k)$. As before, the structural length scale then follows from the space-correlation function.

3 Results

In the following, we present the time evolution of the phase-separated morphologies of binary mixtures in response to a gradual composition quench using kMC simulations, and in response to a gradual temperature quench using both kMC and MD simulations. In section 3.4 we combine the results and discuss their universality.

3.1 Composition quenches (kMC)

We have performed simulations of concentration quenches at both critical ($\Gamma_{\theta, \text{A}} = \Gamma_{\theta, \text{B}}$) and off-critical ($2\Gamma_{\theta, \text{A}} = \Gamma_{\theta, \text{B}}$) compositions, with rates varying from $\Gamma_{\theta} = \Gamma_{\theta, \text{A}} + \Gamma_{\theta, \text{B}} = 3 \cdot 10^{-7}$ to $3 \cdot 10^{-3}$ in units of the hop rate under dilute conditions, ν . In these simulations, the repulsive interaction energy between the two species was $\epsilon_{\text{AB}} = 3k_{\text{B}}T$. Figure 1 shows representative morphologies of both a critical and an off-critical composition for the slowest quench. In both cases, no structure seems discernible at early times. As time proceeds, the surface coverage increases and the constituents phase separate via surface diffusion. For the off-critical mixture, the morphology contains droplets and for the critical mixture it shows a bicontinuous-like structure. Other than that, the time development of their characteristic length scales

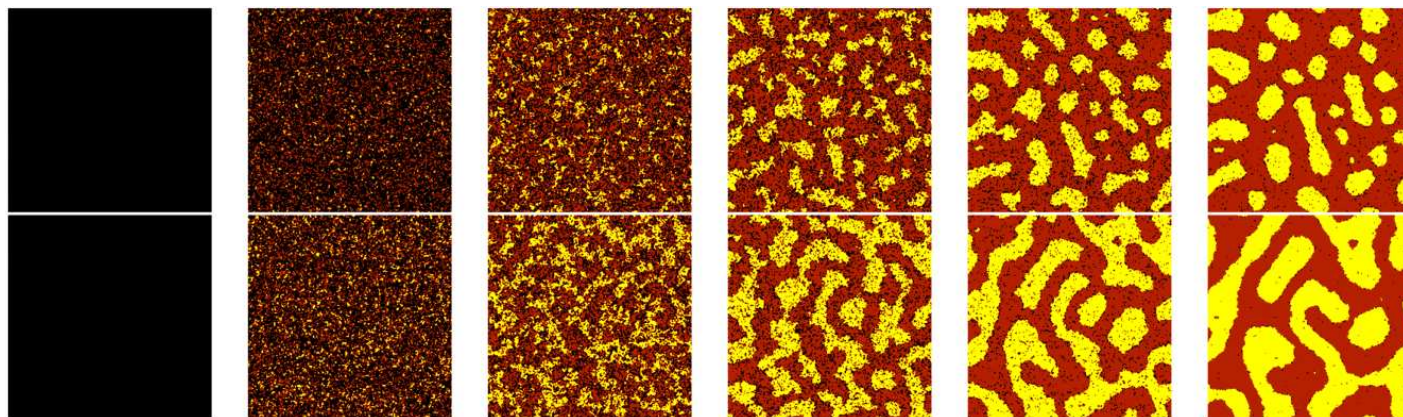


Fig. 1 Time evolution of the structure during a concentration quench (left to right) for an off-critical (top) and a critical composition (bottom). The quench rate is $\Gamma_\theta/v = 3 \cdot 10^{-7}$.

are similar. At the late stages, the coverage reaches unity and the number of vacant sites for molecules to hop into decreases so that a final morphology ‘freezes’ in. This final structure becomes finer with an increasing quench rate. This observation was seen experimentally as well, and was interpreted as a result of less time available for Ostwald ripening⁴⁷.

Here, however, the time for structural coarsening is limited and the quench-rate dependence of the structural length is strongly affected by the early-stage structure development. Crucially, with early-stage structure development we here refer to pre-transitional structuring prior to reaching the binodal, rather than spinodal decomposition after crossing the spinodal. We address this effect by (i) determining the binodal concentration and (ii) by probing both the concentration and the characteristic length scale as a function of time. We have determined the binodal concentration ($\theta \approx 0.63$) from the phase diagram in the top panel of Figure 2[‡]. In that figure, the arrows indicate the trajectory of the examples of Figure 1.

The structural length, R_* , as a function of time at those trajectories we present in the bottom panel of Figure 2 (the statistics are enhanced by performing simulations for 20 random seeds per quench). The length scale is given in units of the lattice spacing, and time is rendered dimensionless using the quench rate. The vertical line indicates the time at which the unstable region of the phase diagram is entered. This figure shows that the morphology is finer for faster quenches not only when the system is frozen, but is finer already at the moment that the miscibility gap of the phase diagram is entered. This implies that the pre-transitional structure development (i.e., in the single-phase region of the phase diagram) crucially affects the emerging morphology after crossing the binodal. The dependence of the structural length of the emerging structure on the quench rate is shown in Figure 7, and will be discussed in section 3.4.

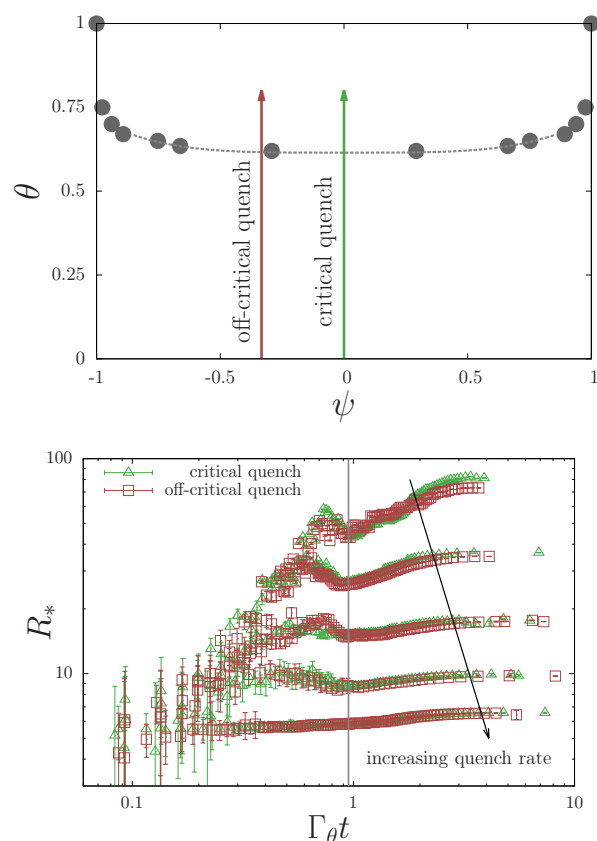


Fig. 2 Top: Phase diagram for lateral interactions $\epsilon_{AB}/k_B T = 3$, with θ the surface coverage and ψ the order parameter. The symbols are the binodal values as obtained by regular Monte Carlo simulations²³. The dashed line is drawn as a guide to the eye. Bottom: Structural length scale R_* as a function of scaled time $v_\theta t$ for various quench rates $\Gamma \propto v_\theta$. The vertical line indicates the time at which the binodal is crossed.

3.2 Temperature quenches (kMC)

Quantifying the early-stage structure development in composition-quench simulations is somewhat obstructed by the noise imposed by the adsorption of species at random lattice sites. This is prevented by keeping the concentration constant, and destabilising the mixture through cooling instead. Indeed,

[‡] We have calculated the phase diagrams using two isolated lattices with a fixed concentration, and an initialised composition. Using a standard Monte Carlo procedure, species are swapped between the two lattices with the appropriate acceptance probability. After sufficient steps, the compositions of the two lattices converge to the coexistence values²³.

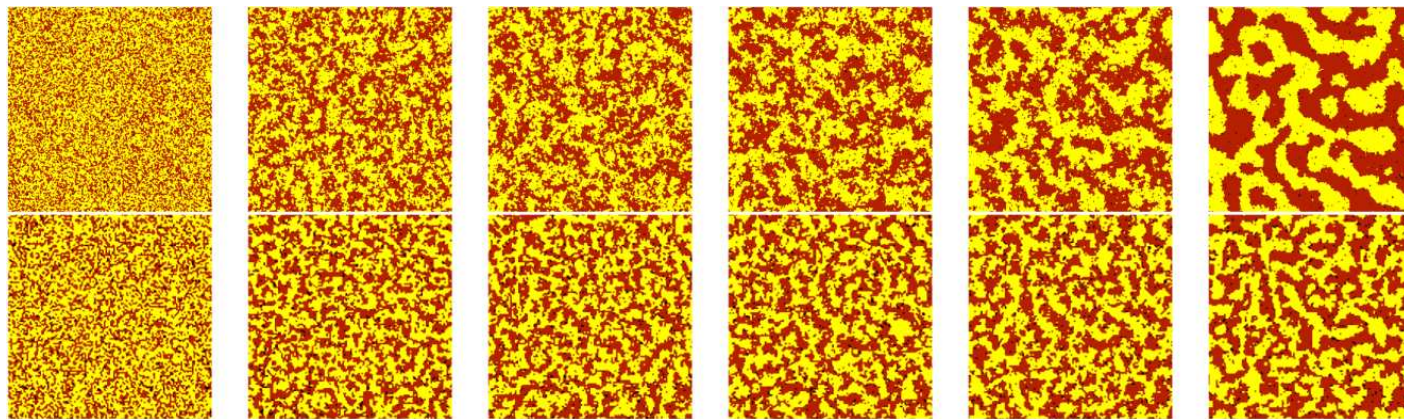


Fig. 3 Time evolution (left to right) of the morphology during a slow (top, $\Gamma_T = 10^{-8}$) and a fast (bottom, $\Gamma_T = 10^{-6}$) temperature quench, as obtained from kMC simulations.

in this section we perform kMC simulations of binary lattice mixtures that phase separate under gradual cooling.

We have chosen the parameter values in the simulations with applications in heterogeneous metal catalysis in mind: For a lattice model to be physically realistic at the molecular scale, the activation energy for a hop of an adsorbant from one site to the other should always be larger than $k_B T$. Assuming an activation energy that depends on the lateral interactions as mentioned below Eq. 17, the interactions between species A and B should be sufficient weak. Because of this Arrhenius-type activation barrier, the diffusivity decreases exponentially with a decreasing temperature. Given these constraints, we have used surface coverages $\theta_A = \theta_B = 0.475$, an activation energy $E_{\text{act}}^0 = 4.2k_B T_0$, and a repulsive interaction energy $\varepsilon_{AB} = 0.8k_B T_0$ at $t = 0$. For these values, phase separation sets in when $\varepsilon_{AB}/k_B T > 1$, which is achieved by decreasing the temperature as $T/T_0 = 1 - \Gamma_T t$. The cooling rate, Γ_T , ranges from 10^{-8} to 10^{-6} in units of the bare hop rate ν .

In Figure 3 we show representative examples of the morphology development during the fastest and the slowest quench. In analogy with the concentration-quenched mixture, the final structure becomes coarser for slower quenches. Like before, we distinguish between early- and late-stage structure development using the time at which the miscibility gap of the phase diagram is entered. The top panel of Figure 4 shows the phase diagram for various surface coverages. For the surface coverage of $\theta = 0.95$ that we study here, the critical temperature is given by $\varepsilon_{AB}/k_B T \approx 1$, which for $\varepsilon_{AB}/k_B T_0 = 0.8$ is reached at time $t = 0.2/\Gamma_T$.

This time is indicated by the vertical line in the bottom panel of Figure 4. This figure shows the time evolution of the characteristic length scale, R_* , of the morphologies (averaged over 20 random seeds per quench). If the temperature would be fixed at the critical temperature, one would expect the structural length scale to increase with the $4/15$ power of time^{27,35,36}. Despite the fact that our simulations have a transient temperature, we do recover this power law (grey lines) for early times. After entering the miscibility gap, the purity of the phase separated domains increases (see Figure 3), but the size of the domains promptly arrests as the mixture freezes at low temperatures. The dependence of the structural length of the emerging structure on the quench

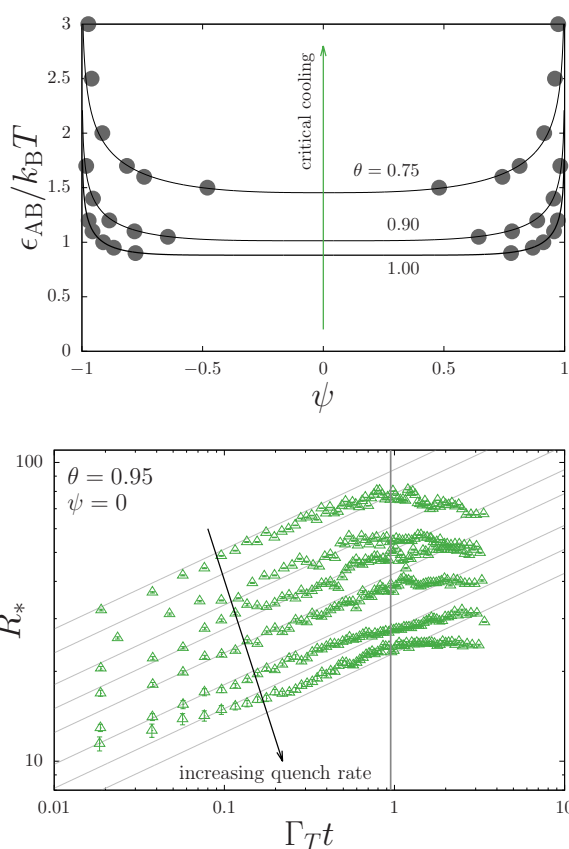


Fig. 4 Top: Phase diagrams for various surface coverages θ . ε_{AB} is the nearest-neighbour interaction energy between species A and B, $k_B T$ is the thermal energy, and ψ is the order parameter. The symbols are the binodal values as obtained by regular Monte Carlo simulations²³. The solid black line represents the Ising model, and the dashed lines are drawn as a guide to the eye. The arrows indicate temperature quenches. Bottom: Time evolution of the characteristic length scale, R_* , for various quench rates. The vertical line indicates the time at which the binodal is crossed.

rate is shown in Figure 7, and will be discussed in section 3.4.

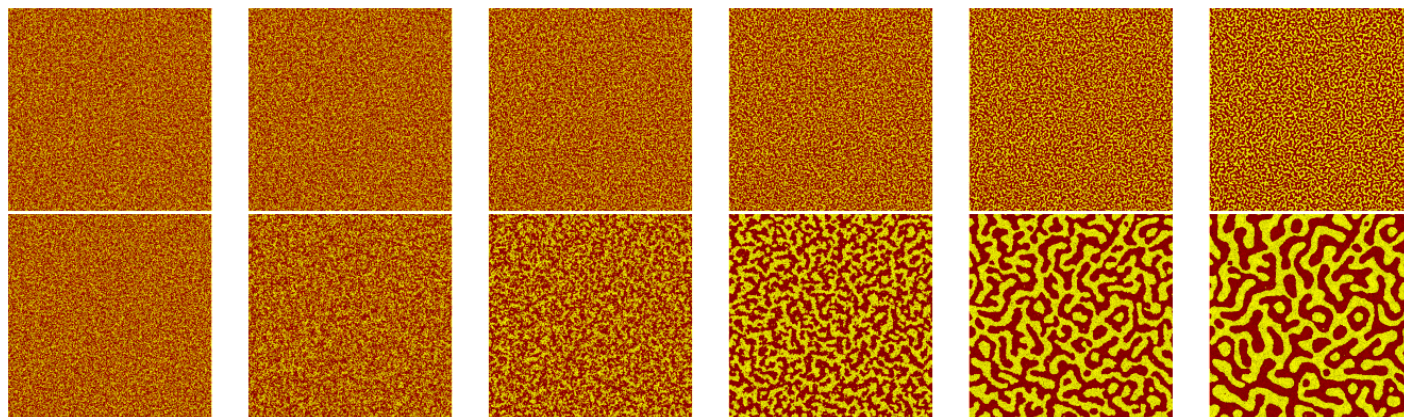


Fig. 5 Time evolution (left to right) of the morphology during a slow (top) and a fast (bottom) temperature quench, as obtained from MD simulations.

3.3 Temperature quenches (MD)

The constraints imposed by the strong temperature-dependence of the mobility as well as the geometry of the lattice are lifted in a natural way by resorting to (Langevin) molecular dynamics (MD) simulations. Indeed, we have conducted MD simulations of a binary mixture with $\epsilon_{AB} = 1$ in Lennard-Jones unit energy ϵ . In these simulations, we have initialised the structure at temperature $T_0 = 2.5\epsilon$, and have decreased the temperature to $T_{\text{final}}/T_0 = 1 - \Gamma_T t_{\text{final}} = 0.2$ linearly in time with Γ_T varying from $3.2 \cdot 10^{-4}$ to $3.2 \cdot 10^{-6}$.

Figure 5 shows representative images of the time evolution of the morphology for quench rates of $3.2 \cdot 10^{-4}$ and $3.2 \cdot 10^{-6}$. These morphologies are qualitatively similar to those found in the kMC simulations of temperature quenched binary mixtures (see Figure 3). Indeed, some early-stage coarsening is visible, as well as purification of the domains at late times. In contrast to the kMC simulations, the constituents remain mobile and coarsening proceeds at the late stages. By fitting the late-stage coarsening exponent, $R_* \propto (t - \tau)^{1/3}$, with τ the time at which late-stage coarsening sets in, we extract τ and estimate the critical temperature below which phase separation takes place.

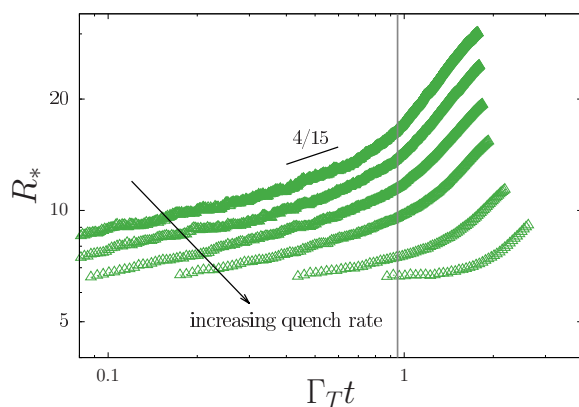


Fig. 6 Time evolution of the characteristic length scale, R_* , for quench rates ranging from $3.2 \cdot 10^{-6}$ to $3.2 \cdot 10^{-4}$. The vertical line indicates the (approximate) time at which the binodal is crossed.

The time at which this happens is indicated by the vertical line

in Figure 6. This figure shows the characteristic length scale, R_* , (in units of Lennard-Jones length scale σ) as a function of time. We have rendered the time dimensionless using a quench rate that we estimated by comparing the time scale of phase separation in Figure 6 to those in Figure 4. Like before, R_* increases at early times reasonably consistently with the 4/15th power of time up to the time where the critical temperature is reached. After that, true phase separation and coarsening of the emerging structure sets in.

3.4 Universal scaling

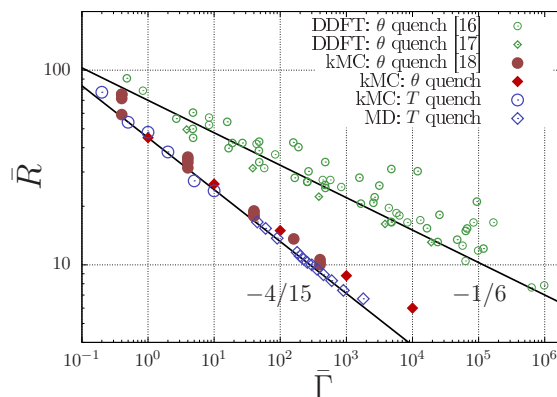


Fig. 7 Dimensionless length scale, \bar{R} , of emerging structures as a function of the dimensionless quench rate, $\bar{\Gamma}$, as calculated using density functional theory (DDFT)^{21,22}, kinetic Monte Carlo (kMC) lattice simulations²³, as well as Langevin molecular dynamics (MD) simulations. The results were collected for temperature (T) and concentration (θ) quenches and for various numbers of components; see main text for more detail. The lines with slopes $-1/6$ and $-4/15$ represent the expected results from mean-field theory¹⁷ and critical dynamics²⁷, respectively.

For all three types of simulations of binary mixtures above, the emerging structure is determined by the correlation length, $\bar{R} \equiv R_*(\tau)$, at the point in time, τ , where the miscibility gap of the phase diagram is entered. In Figure 7 we plot this quantity as a function of the (scaled) quench rate for all simulations, and compare this to the results of earlier reported kMC simulations of

a single-component phase-separating mixture²³ and for dynamic density functional theory (DDFT) simulations of phase separating binary²¹ and ternary²² mixtures. All of those reported works studied phase separation in response to a concentration rather than a temperature quench. The \bar{R} values of the DDFT results, as well as the quench rates $\bar{\Gamma}$ have been shifted for clarity.

From Figure 7 we see that the microscopic modelling results using kMC and MD show a much stronger dependence ($-4/15$) on the quench rate than the DDFT calculations do ($-1/6$). While the power $-1/6$ is expected from mean-field theory (see section 2.1), the power $-4/15$ agrees with the fast-quench limit of pretransitional structuring in Eq. 15.

4 Conclusion

In this work, we have proposed a mechanism of phase separation in continuously quenched systems, which addresses the failure of mean-field theory under these conditions. In this mechanism, 'pretransitional structuring' due to critical fluctuations takes place prior to reaching the miscibility gap. In a slow-quench regime, the emerging length scale is dictated by a correlation length that can be understood in terms of equilibrium fluctuations. This limit of the theory has provided an excellent agreement with the experiments in Ref.⁶. On the other hand, in a fast-quench limit the emerging length scale is determined by an out-of-equilibrium correlation length that is determined by dynamic critical scaling.

The slow-quench limit was inaccessible in our kinetic Monte Carlo (kMC) and molecular dynamics (MD) simulations of a binary fluid in response to a homogeneous concentration and temperature quench. However, these simulations did show a clear breakdown of mean-field theory, and an excellent agreement with the fast-quench limit of our theory.

While our simulation results are strictly limited to two-dimensional binary fluids with local conservation laws (i.e., 'Passive Model B')³⁹, our conclusions can be extrapolated to various three-dimensional examples with different types of critical dynamics²⁷, and in either the slow- or fast-quench limit see Table 1. Indeed, some applications in soft-matter science with Model A dynamics include reaction-diffusion mixtures with (reversible) chemical reactions^{10–13,40,41}, as well as liquid crystals^{2–4}. Phase-separation phenomena in active matter (i.e., mixtures of active / self-propelling particles) are governed by 'Active Model B' dynamics^{5,48}. From Table 1, we expect that in both Model A and Active Model B kinetics the quench rate is even of stronger influence to the emerging morphology than in the Passive Model B kinetics examples that we have studied so far. We hope that the present work will assist the experimental and theoretical research to phase-separation phenomena under transient conditions in the fields of both biophysics and materials science.

Conflicts of interest

There are no conflicts to declare.

Acknowledgements

C.S. and T.C.B.M acknowledge the Engineering and Physical Sciences Research Council (Grant No. EP/N031431/1) for funding. S.P. acknowledges the Brandeis MRSEC and XSEDE for funding

Table 1 Values of the scaling exponents α for power law $R_0 \propto \Gamma^{-\alpha}$, with R_0 the emerging length scale of phase-separating morphologies and Γ the quench rate. In the slow-quench limit $\alpha = \nu/(3\nu + \nu^* + 1)$ with $\nu^* = \nu(1 + z - d)$, and in the fast-quench limit $\alpha = 1/z$. In 2D, $d = 2$ and $\nu = 1$ and in 3D, $d = 3$ and $\nu \approx 0.63$. The value of z depends on d and on the type of model used.

	slow 2D	slow 3D	fast 2D	fast 3D
Model A	0.19	0.22	0.46	0.49
Passive Model B	0.15	0.18	4/15	0.326
Active Model B	0.22	0.22	0.62	0.5

and computer time, and Michael F. Hagan for valuable discussions.

Notes and references

- 1 Y. Shin and C. P. Brangwynne, *Science*, 2017, **357**, 1253.
- 2 J. K. G. Dhont and W. J. Briels, *Phys. Rev. E*, 2005, **72**, 031404.
- 3 M. P. Lettinga, K. Kang, P. Holmqvist, A. Imhof, D. Derks and J. K. G. Dhont, *Phys. Rev. E*, 2006, **73**, 011412.
- 4 M. J. Green, R. A. Brown and R. C. Armstrong, *J. Non-Newtonian Fluid Mech.*, 2009, **161**, 30–36.
- 5 R. Wittkowski, A. Tiribocchi, J. Stenhammar, R. J. Allen, D. Marenduzzo and M. E. Cates, *Nature Comm.*, 2014, **5**, 4351.
- 6 M. Rüllmann and I. Alig, *J. Chem. Phys.*, 2004, **120**, 7801–7810.
- 7 J.-P. Hansen and I. R. McDonald, *Theory of simple liquids*, Academic Press, Hoboken, NJ, 3rd edn, 2006.
- 8 C. J. Brabec, S. Gowrisanker, J. J. M. Halls, D. Laird, S. Jia and S. P. Williams, *Adv. Mater.*, 2010, **22**, 3839–3856.
- 9 H. Tanaka, *J. Phys.: Condens. Matter*, 2000, **12**, R207–R264.
- 10 K. Furtado and J. M. Yeomans, *Phys. Rev. E*, 2006, **73**, 066124.
- 11 R. Krishnan and S. Puri, *Phys. Rev. E*, 2015, **92**, 052316.
- 12 S. C. Glotzer, E. A. D. Marzio and M. Muthukumar, *Phys. Rev. Lett.*, 1995, **74**, 2034–2037.
- 13 A. Singh, S. Puri and C. Dasgupta, *J. Phys. Chem. B*, 2012, **116**, 4519.
- 14 P. Perlekar, R. Benzi, H. J. H. Clercx, D. R. Nelson and F. Toschi, *Phys. Rev. Lett.*, 2014, **112**, 014502.
- 15 R. Benzi, M. Bernaschi, M. Sbragaglia and S. Succi, *Eur. Phys. J. E*, 2011, **34**, 93.
- 16 M. A. Muñoz, *Rev. Mod. Phys.*, 2018, **90**, 031001.
- 17 E. L. Huston, J. W. Cahn and J. E. Hilliard, *Acta Metall.*, 1966, **15**, 1053–1062.
- 18 H.-O. Carmesin, D. Heermann and K. Binder, *Z. Phys. B - Condens. Matter*, 1986, **65**, 89–102.
- 19 E. B. Nauman, M. V. Ariyapadi, N. P. Balsara, T. A. Grocela, J. S. Furno, S. H. Liu and R. Mallikarjun, *Chem. Eng. Comm.*, 1988, **66**, 29–55.
- 20 O. Wodo and B. Ganapathysubramanian, *Comp. Mater. Sci.*, 2012, **55**, 113–126.
- 21 C. Schaefer, P. van der Schoot and J. J. Michels, *Phys. Rev. E*, 2015, **91**, 022602.
- 22 C. Schaefer, J. J. Michels and P. van der Schoot, *Macromolecules*, 2016, **49**, 6858–6870.

- 23 C. Schaefer, *Phys. Rev. Lett.*, 2018, **120**, 036001.
- 24 S. Keßler, F. Schmid and K. Drese, *Soft Matter*, 2016, **12**, 7231–7240.
- 25 S. Qi and F. Schmid, *Macromolecules*, 2018, **50**, 9831–9845.
- 26 E. N. Cirillo, M. Colangeli, E. Moons, A. Muntean, S.-A. Muntean and J. van Stam, *Eur. Phys. J. Special Topics*, 2019, **228**, 55–68.
- 27 P. C. Hohenberg and B. I. Halperin, *Rev. of Mod. Phys.*, 1977, **49**, 435–479.
- 28 H. Cook, *Acta Metall.*, 1970, **17**, 297–306.
- 29 J. S. Langer, *Ann. Phys.*, 1971, **65**, 53–86.
- 30 R. G. Petschek and H. Metiu, *J. Chem. Phys.*, 1983, **79**, 3443–3456.
- 31 J. F. Lutsko, *J. Chem. Phys.*, 2012, **136**, 034509.
- 32 S. Buil, J. P. Delville and A. Ducasse, *Eur. Phys. J. E*, 2000, **2**, 105.
- 33 D. Kashchiev, *Nucleation: Basic theory with applications*, Butterworth-Heinemann, Oxford, 2000.
- 34 K. Binder, *rnal de Physique Colloques*, 1, 1980, **41**, C4–51–C4–62.
- 35 F. J. Alexander, D. A. Huse and S. A. Janowsky, *Phys. Rev. B*, 1994, **50**, 663–667.
- 36 C. Godreche, F. Krzakala and F. Ricci-Tersenghi, *J. Stat. Mech.: Theor. Exp.*, 2004, P04007.
- 37 S. R. de Groot and P. Mazur, *Non-equilibrium Thermodynamics*, Dover Publications, Inc., New York, 1984.
- 38 J. W. Cahn and J. E. Hilliard, *J. Chem. Phys.*, 1958, **28**, 258.
- 39 K. Kawasaki, *Phys. Rev.*, 1965, **145**, 224–230.
- 40 Puri and Frisch, *J. Phys. A: Math. Gen.*, 1994, **27**, 6027–6038.
- 41 Puri and Frisch, *J. Mod. Phys. B*, 1998, **12**, 1623–1641.
- 42 K. Huang, *Statistical Mechanics*, John Wiley & Sons, Inc., Toronto, 2nd edn, 1987.
- 43 C. G. W. Hermse and A. P. J. Jansen, *Kinetics of surface reactions with lateral interactions: Theory and simulations*, The Royal Society of Chemistry, 2006, vol. 19, pp. 109–163.
- 44 A. P. J. Jansen, *An introduction to kinetic Monte Carlo simulations of surface reactions*, Springer-Verlag, Berlin Heidelberg, 1st edn, 2012.
- 45 J. J. Lukkien, J. P. L. Segers, P. A. J. Hilbers, R. J. Gelten and A. P. J. Jansen, *Phys. Rev. E*, 1998, **58**, 2598–2610.
- 46 S. Plimpton, *J. Comp. Phys.*, 1995, **117**, 1–19.
- 47 J. J. van Franeker, D. Werhoff, M. Turbiez, M. M. Wienk, V. Schmidt and R. A. J. Janssen, *Adv. Func. Mater.*, 2015, **25**, 855–863.
- 48 M. Kardar and G. P. Y.-C. Zhang, *Phys. Rev. Lett.*, 1986, **56**, 889–892.